## **OPEN ACCESS**



## Probing the Extragalactic Mid-infrared Background with HAWC

```
A. Albert , R. Alfaro, R. Alvarez, J. C. Arteaga-Velázquez, D. Avila Rojas, H. A. Ayala Solares, R. Babu , R. Babu
   E. Belmont-Moreno<sup>2</sup>, K. S. Caballero-Mora<sup>3</sup>, T. Capistrán<sup>7</sup>, A. Carramiñana<sup>8</sup>, S. Casanova<sup>9</sup>, O. Chaparro-Amaro<sup>10</sup>
U. Cotti<sup>4</sup>, J. Cotzomi<sup>11</sup>, S. Coutiño de León<sup>12</sup>, E. De la Fuente<sup>13</sup>, R. Diaz Hernandez<sup>8</sup>, M. A. DuVernois<sup>12</sup>, M. Durocher<sup>1</sup>
 J. A. Matthews<sup>25</sup>, P. Miranda-Romagnoli<sup>26</sup>, E. Moreno<sup>11</sup>, M. Mostafá<sup>5</sup>, A. Nayerhoda<sup>9</sup>, L. Nellen<sup>27</sup>, M. Newbold<sup>22</sup>, M. U. Nisa<sup>23</sup>, R. Noriega-Papaqui<sup>26</sup>, N. Omodei<sup>28</sup>, A. Peisker<sup>23</sup>, Y. Pérez Araujo<sup>7</sup>, E. G. Pérez-Pérez<sup>24</sup>, C. D. Rho<sup>29</sup>, D. Rosa-González<sup>8</sup>, H. Salazar<sup>11</sup>, D. Salazar-Gallegos<sup>23</sup>, F. Salesa Greus<sup>9,30</sup>, A. Sandoval<sup>2</sup>, J. Serna-Franco<sup>2</sup>, A. J. Smith<sup>14</sup>,
Y. Son<sup>29</sup>, R. W. Springer<sup>22</sup>, O. Tibolla<sup>24</sup>, K. Tollefson<sup>23</sup>, I. Torres<sup>8</sup>, R. Torres-Escobedo<sup>31</sup>, R. Turner<sup>6</sup>, F. Ureña-Mena<sup>8</sup>,
                                         L. Villaseñor<sup>11</sup>, X. Wang<sup>6</sup>, T. Weisgarber<sup>12</sup>, E. Willox<sup>14</sup>, H. Zhou<sup>4</sup>, and C. de León<sup>4</sup>
                                                                                                                   HAWC Collaboration
                                                       <sup>1</sup> Physics Division, Los Alamos National Laboratory, Los Alamos, NM, USA; mkf5479@psu.edu
                                                           <sup>2</sup> Instituto de Física, Universidad Nacional Autónoma de México, Ciudad de México, México
                                                                              Universidad Autónoma de Chiapas, Tuxtla Gutiérrez, Chiapas, México
                                                                             <sup>4</sup> Universidad Michoacana de San Nicolás de Hidalgo, Morelia, México
                                                                   <sup>5</sup> Department of Physics, Pennsylvania State University, University Park, PA, USA
                                                                   Department of Physics, Michigan Technological University, Houghton, MI, USA
                                                      7 Instituto de Astronomía, Universidad Nacional Autónoma de México, Ciudad de México, México
                                                                               Instituto Nacional de Astrofísica, Óptica y Electrónica, Puebla, México
                                                        <sup>9</sup> Institute of Nuclear Physics Polish Academy of Sciences, PL-31342 IFJ-PAN, Krakow, Poland <sup>10</sup> Centro de Investigación en Computación, Instituto Politécnico Nacional, México City, México
                                              11 Facultad de Ciencias Físico Matemáticas, Benemérita Universidad Autónoma de Puebla, Puebla, México
12 Department of Physics, University of Wisconsin-Madison, Madison, WI, USA
                        Departamento de Física, Centro Universitario de Ciencias Exactas e Ingenierias, Universidad de Guadalajara, Guadalajara, México

14 Department of Physics, University of Maryland, College Park, MD, USA
                                                                     <sup>15</sup> Gran Sasso Science Institute (GSSI), Via Iacobucci 2, I-67100, L'Aquila, Italy
                                      <sup>16</sup> Istituto Nazionale di Fisica Nucleare (INFN) Laboratori Nazionali del Gran Sasso, I-67100 Assergi, L'Aquila, Italy
                  17 Tecnologico de Monterrey, Escuela de Ingeniería y Ciencias, Avenida Eugenio Garza Sada 2501, Monterrey, Nuevo León, 64849, México
                                                                             Max-Planck Institute for Nuclear Physics, D-69117 Heidelberg, Germany
                        <sup>19</sup> Department of Physics, Faculty of Science, Chulalongkorn University, 254 Phayathai Road, Pathumwan, Bangkok 10330, Thailand
                               National Astronomical Research Institute of Thailand (Public Organization), Don Kaeo, MaeRim, Chiang Mai 50180, Thailand
                                          Erlangen Centre for Astroparticle Physics, Friedrich-Alexander-Universität Erlangen-Nürnberg, Erlangen, Germany
                                                                   Department of Physics and Astronomy, University of Utah, Salt Lake City, UT, USA
                                                            <sup>23</sup> Department of Physics and Astronomy, Michigan State University, East Lansing, MI, USA
                                                                                             <sup>4</sup>Universidad Politecnica de Pachuca, Hidalgo, México
                                                              Dept of Physics and Astronomy, University of New Mexico, Albuquerque, NM, USA
26 Universidad Autónoma del Estado de Hidalgo, Pachuca, México
                                              <sup>27</sup> Instituto de Ciencias Nucleares, Universidad Nacional Autónoma de México, Ciudad de México, México

<sup>28</sup> Department of Physics, Stanford University, Stanford, CA 943054060, USA

<sup>29</sup> Hairardin of Spaul, Spau
                                                                                                     University of Seoul, Seoul, Republic of Korea
                                                    <sup>30</sup> Instituto de Física Corpuscular, CSIC, Universitat de València, E-46980, Paterna, Valencia, Spain
                    <sup>31</sup> Tsung Dao Lee Institute and School of Physics and Astronomy, Shanghai Jiao Tong University, Shanghai, People's Republic of China
                                                      Received 2022 February 28; revised 2022 May 18; accepted 2022 June 7; published 2022 July 18
```

### **Abstract**

The extragalactic background light (EBL) contains all the radiation emitted by nuclear and accretion processes in stars and compact objects since the epoch of recombination. Measuring the EBL density directly is challenging, especially in the near-to-far-infrared wave band, mainly due to the zodiacal light foreground. Instead, gamma-ray astronomy offers the possibility to indirectly set limits on the EBL by studying the effects of gamma-ray absorption in the very high energy (VHE: >100 GeV) spectra of distant blazars. The High Altitude Water Cherenkov Gamma Ray Observatory (HAWC) is one of the few instruments sensitive to gamma rays with energies above 10 TeV. This offers the opportunity to probe the EBL in the near/mid-IR region:  $\lambda = 1$ –100  $\mu$ m. In this study, we fit physically motivated emission models to Fermi-LAT gigaelectronvolt data to extrapolate the intrinsic teraelectronvolt spectra of blazars. We then simulate a large number of absorbed spectra for different randomly generated EBL model shapes and calculate Bayesian credible bands in the EBL intensity space by comparing and testing the agreement

between the absorbed spectra and HAWC extragalactic observations of two blazars. The resulting bands are in agreement with current EBL lower and upper limits, showing a downward trend toward higher wavelength values  $\lambda > 10~\mu m$  also observed in previous measurements.

Unified Astronomy Thesaurus concepts: Gamma-ray astronomy (628); Diffuse radiation (383); Blazars (164)

### 1. Introduction

The extragalactic background light (EBL) comprises all radiation released by nuclear and accretion processes since the epoch of recombination. It consists of all emitted radiation from stars and compact object surroundings, including that absorbed/re-emitted by dust and accumulated over all redshifts. Measuring and constraining this background radiation is crucial to understanding star formation processes and galaxy evolution models. Our current knowledge of EBL is limited, and its direct measurements are challenging due to foreground contamination coming, mainly, from zodiacal light. However, upper and lower limits have been established using various methods, e.g., integrated galaxy counts from optical observations with the Hubble Space Telescope (Gardner et al. 2000; Madau & Pozzetti 2000) and infrared (IR) observations using the Spitzer Space Telescope (Fazio et al. 2004; Papovich et al. 2004) and the Infrared Space Observatory (Elbaz et al. 2002), as well as IR background empirical determinations based on deep galaxy surveys (Stecker et al. 2016). An extensive discussion on EBL-related matters can be found in Elbaz et al. (2002), Orr et al. (2011), and Cooray (2016).

Over the past two decades, VHE gamma-ray observations have been used to help constrain the spectral properties of EBL. particularly with observations from blazars, a subtype of active galactic nuclei (AGN) with ultra-relativistic jets oriented close to the observer's line of sight. VHE gamma rays coming from blazars interact via pair production with EBL photons (Gerasimova et al. 1962; Gould & Schréder 1967) producing imprints in the observed energy spectra of distant sources. These imprints, along with intrinsic spectral assumptions, can be used to derive limits on the EBL near/mid-IR range using VHE observations of blazars (e.g., Aharonian et al. 2007; Mazin & Raue 2007; Orr et al. 2011; Biteau & Williams 2015; Abdalla et al. 2017; Abeysekara & Archer 2019; Acciari & Ansoldi 2019). The gamma-ray horizon establishes the energy at which the intensity of radiation is diminished by a factor of 1/e with respect to the emitted intensity. This energy value depends on the distance of the source and it needs to be taken into account when selecting suitable candidate sources for this type of study. If the source is too close, the absorption effect will only be measurable at higher energies, where, depending on the detector and the energy of the gamma ray, the sensitivity might be too low. On the other hand, distant sources will be dimmer, precisely due to the EBL absorption, so these are not ideal candidates to work with either (Franceschini et al. 2019). Equation (1) approximately relates the energy of a gamma ray  $(E_{\gamma})$  with the wavelength range of the EBL radiation  $(\lambda_{\rm EBL})$ involved in the pair production interaction:

$$\lambda_{\rm EBL} \sim [0.5 \mu {\rm m} - 5 \mu {\rm m}] \times \left(\frac{E_{\gamma}}{1 \, {\rm TeV}}\right) \times (1 + z)^2, \qquad (1)$$

where z is the redshift of the source emitting the gamma ray. This equation is useful to estimate the EBL probing power when considering a specific source observed with a specific instrument.

The High-Altitude Water Cherenkov Gamma Ray Observatory (HAWC) is a water Cherenkov detector that has been operational since 2015 (further technical details can be found in Section 2) and has detected extragalactic sources significantly up to 10 TeV (Albert et al. 2022). This energy is close to the one established by the gamma-ray horizon for sources like the two blazars Markarian 501 (Mrk 501) and Markarian 421 (Mrk 421; hereafter collectively referred to as Markarians), putting HAWC in an advantageous position to potentially probe the mid-IR region of EBL using observations from these sources.

In this study, physically motivated emission models and data from the Fermi-LAT are used to construct an intrinsic spectrum for each of the Markarians (see Section 3.1). A large number of randomly generated EBL model shapes are used to apply the EBL attenuation effect to these intrinsic spectra to compare with HAWC data (see Section 3.2). The comparison is performed using threeML: a software package for likelihood fitting, Vianello et al. (2015), in a way that each EBL model can be assigned a likelihood value that expresses the agreement between that particular spectral realization and HAWC data (see Section 3.3). This method has the advantage of being independent of any particular EBL shape and of assuming physically motivated intrinsic spectral properties for the sources. Finally, weights are applied to each model in accordance with their calculated likelihood value, and credible intervals in the EBL spectral energy distribution space are derived (Section 4).

## 2. Data: HAWC and Fermi-LAT

HAWC is an array of 300 water Cherenkov detector tanks located in Sierra Negra, México, at an altitude of 4100 m above sea level and covering a total area of 22,000 m<sup>2</sup>. Each tank has four photomultiplier tubes (PMTs) facing upward that can detect Cherenkov light in the water from the transit of secondary particles, which are produced by gamma rays and cosmic rays interacting with the atmosphere. HAWC triggers at a rate of 25 kHz and has a duty cycle of >95%. The observatory continuously monitors 2/3 of the sky, detecting gamma rays in the energy range between 100 GeV and several hundred teraelectronvolts. More information on the HAWC Observatory operation, performance, and the way air shower event data are reconstructed can be found in Abeysekara & Albert (2017). For this analysis, specific Fermi-LAT and HAWC data from the blazars Mrk 421 (z = 0.031) and Mrk 501 (z = 0.034) were selected (redshift sourced from NED<sup>32</sup>). These are two extensively studied extragalactic sources and the brightest in the teraelectronvolt band. Both sources have been significantly detected by HAWC above 300 GeV up to 10 TeV (Albert et al. 2022) and by Fermi-LAT between 100 MeV and 1 TeV (Abdo et al. 2011; Abdo & Ackermann 2011). For the HAWC data set, 1343 days of data were used, taken between 2015 June and 2019 June (Abeysekara et al. 2019). The

<sup>&</sup>lt;sup>32</sup> The NASA/IPAC Extragalactic Database (NED) is operated by the Jet Propulsion Laboratory, California Institute of Technology, under contract with the National Aeronautics and Space Administration.

analysis was performed using maps created with a special algorithm for reconstructing and determining the energy of the primary gamma rays. This algorithm, denominated ground parameter algorithm, is based primarily on the charge density at a fixed optimal distance from the shower axis and it divides the energy range into quarter-decade bins in log 10(E), beginning at  $\log(E/\text{TeV}) = -0.5 \text{ (0.316 TeV)}$  and ending at  $\log(E/\text{TeV})$ TeV) = 2.5 (316 TeV). The ground parameter energy estimator was chosen because it is optimal for higher energies, between 10 and 316 TeV (Abeysekara et al. 2019), where the instrument could potentially probe the EBL mid-IR region. For the Fermi-LAT data set, a time period corresponding to the HAWC data set was selected between 57180 and 58640 MJD. This data set is within the energy range of 100 MeV-316 GeV, where the absorption is, at most, around 5% for the Markarians' redshift.<sup>33</sup> The Fermi-LAT analysis is described in more detail in Section 3.1.

## 3. EBL Analysis

The approach adopted in this study consists of calculating EBL intensity limits by comparing the expected absorbed flux with actual HAWC observations. The method is similar to previous EBL studies: Mazin & Raue (2007), Orr et al. (2011), Biteau & Williams (2015), and in particular, to that of Abeysekara & Archer (2019), presented by the VERITAS Collaboration. In the latter analysis, a large number of randomly generated EBL models is used to calculate the corresponding de-absorbed spectra of selected blazars, and then each model is weighted using criteria based on intrinsic assumptions for these sources to finally derive limits to the EBL intensity. In the present analysis, the EBL models are used to simulate the absorption effect, which is then applied over the assumed intrinsic spectra. The resulting absorbed spectra are then compared to the real HAWC data by calculating a likelihood value. Finally, each EBL model is weighted according to its corresponding likelihood value.

## 3.1. Intrinsic Spectra: Fermi-LAT and Naima

A possible and reasonable assumption is to consider the intrinsic teraelectronvolt spectrum of a given source as an extension of a physical emission model that is in agreement with gigaelectronvolt observations. This assumption relies on the fact that gamma rays in the high energy regime (HE; 100 MeV–100 GeV) and relatively low redshifts ( $z \lesssim 0.1$ ) are not significantly affected by EBL absorption, and therefore the observed spectrum can be safely considered to be practically the same as the intrinsic one (e.g., Abdo et al. 2010; Orr et al. 2011; Furniss et al. 2013). In the present study, a Fermi-LAT standard fitting analysis was performed to obtain spectral flux points corresponding to Mrk 421 and Mrk 501, using observations from a similar time period as the one observed by HAWC (for details see Section 2). The Fermi-LAT analysis was carried out using the instrument response function P8R2\_SOURCE\_V6, and the spectral parameters are estimated by the binned maximum-likelihood method using the Fermipy v0.17.3 package, Wood et al. (2017). The analysis was also performed with a zenith cut of 90°, and as mentioned in Section 2, within the energy range of 100 MeV-316 GeV to minimize possible absorption effects while including as much

Table 1

Electron Distribution Parameters Resulting from the SSC Emission Model
Likelihood Fit Performed with Naima to Fermi-LAT Data from Mrk 421 and
Mrk 501

Parameter	Mrk 421	Mrk 501
$\alpha$ $E_c$ (TeV) $A$ (1/eV)	$2.77 \pm 0.02$ $(1.2 \pm 0.9) \times 10^{1}$ $(1.4 \pm 0.1) \times 10^{36}$	$\begin{array}{c} 2.75 \pm 0.04 \\ (1.85 \pm 0.75) \times 10^{1} \\ (0.9 \pm 0.1) \times 10^{36} \end{array}$

**Note.** A is a normalization factor,  $E_0$  is a reference energy set at 1 TeV,  $\alpha$  is the power-law index, and  $E_c$  is the cutoff energy.

data as possible. The events were extracted within a 10° region of interest centered on each source position. The background model includes sources from the Preliminary Fermi-LAT 8 yr point-source catalog, <sup>34</sup> Galactic diffuse emission *glliemv06.fits* and the isotropic diffuse emission *isoP8R2SOURCEV6v06.txt* models.

To avoid an overestimation of the intrinsic flux, each source's lowest energy flux point observed by HAWC (Albert et al. 2022) is used as a guide; observed Mrk 421 and Mrk 501 flux points at an energy of 830 and 750 GeV, respectively, are de-absorbed according to Franceschini et al. (2008) model. These de-absorbed flux points are included in the set of flux points obtained from the Fermi-LAT analysis described above, and altogether are used to fit a physically motivated emission model with Naima: a python software that calculates the nonthermal emission from a leptonic or hadronic population of particles, Zabalza (2015).

In this case, the data set is fit with a synchrotron-self-Compton (SSC) model, a scenario in which synchrotron radiation is produced by electrons moving at relativistic velocities in randomly oriented magnetic fields and upscattered by inverse Compton into higher energies by the same electron population. The leptonic distribution is chosen to follow an exponentially cutoff power-law (ECPL) distribution:

$$f(E) = A \left(\frac{E}{E_0}\right)^{-\alpha} \exp\left(-\frac{E}{E_c}\right). \tag{2}$$

where A is a normalization factor,  $E_0$  is a reference energy set at 1 TeV,  $\alpha$  is the power-law index, and  $E_c$  is the cutoff energy. The decision for this particular leptonic distribution is motivated by other studies performed on the Markarians by HAWC (Albert et al. 2022) and others (Zhu et al. 2016; Abdo & Ackermann 2011). Based on the results reported in Albert et al. (2022) the magnetic field and emission radius values are set at 0.03 G and  $4 \times 10^{16}$  cm for Mrk 421 and 0.02 G and  $1 \times 10^{17}$  cm for Mrk 501, respectively. Table 1 shows the best-fit parameters for the electron distributions of each source. The best-fit models are then extrapolated into teraelectronvolt energies (see Figure 2) and used as templates for the intrinsic spectra of the sources (see Section 3.3).

## 3.2. EBL Models

To generate different EBL model shapes, a grid of 12  $\lambda$  values across the wavelength of the EBL photons between 1 and 100  $\mu$ m is set. For each  $\lambda$  value, an intensity (nW m<sup>-2</sup> sr<sup>-1</sup>) value is assigned by randomly generating a number

<sup>33</sup> Estimated assuming the Domínguez & Primack (2011) EBL model.

https://fermi.gsfc.nasa.gov/ssc/data/access/lat/fl8y/

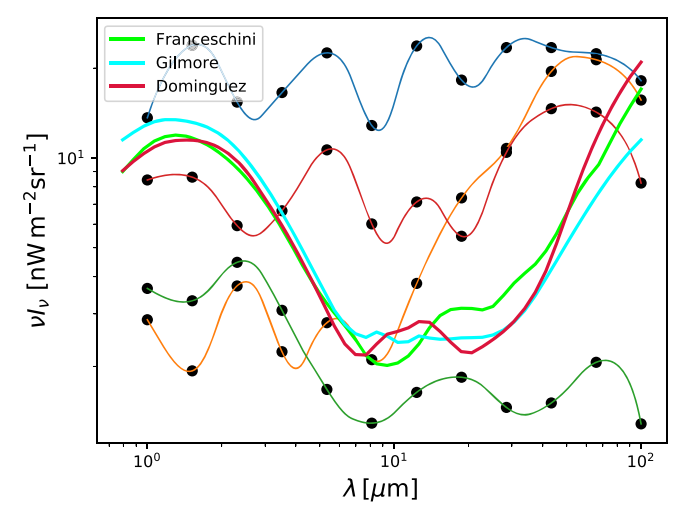


Figure 1. Sample of spline-interpolated models in the EBL spectral density space. Also shown are the Franceschini et al. (2008), Domínguez et al. (2011) and Gilmore et al. (2012) EBL models shapes.

between 1 and 50 nW m<sup>-2</sup> sr<sup>-1</sup>, resulting in a flat initial distribution in EBL intensity; the range is chosen to contain the EBL upper and lower limits discussed in Section 1. A particular EBL shape is defined by interpolating each intensity point corresponding to each wavelength, using second-order splines. To avoid sharp model shapes, the intensity at consecutive grid points is not allowed to change by more than a factor of 2. For this reason, and since the interpolation is performed in increasing order in  $\lambda$ , intensities for higher  $\lambda$ values are more conditionally sampled than lower  $\lambda$  values. This bias is then corrected by weighting the intensities in each grid point to recover the initial flat intensity distribution. Avoiding sharp models that are nonphysical has the caveat of neglecting possible features coming from polycyclic aromatic hydrocarbons, known to be present in the mid-IR range (Lagache et al. 2005). However, for relatively small redshifts, like those considered in this analysis, these sharp features would be smoothed out to a bump (Domínguez et al. 2011). Figure 1 shows examples of EBL shapes generated in this way. A total of 30,000 models are generated at redshift z = 0. The EBL intensity can be then used to compute the optical depth  $\tau(E, z)$ , which quantifies the absorption effect of gamma rays with energy (E) and traveling a given distance associated with a redshift value z. The theoretical framework behind these calculations can be found in, e.g., Dwek & Krennrich (2013), Biteau & Williams (2015), and Abdalla et al. (2017). In this analysis, the  $\tau$  values are computed using the ebltable python package: a tool to read in and interpolate tables for EBL density and to calculate the resulting opacity for highenergy gamma rays. The  $\tau$  values are computed between 0.1 and 50 TeV and for redshifts between 0.03 and 0.04, chosen respectively to include the Markarians' highest energy points measured by HAWC and their redshift. The points at which the calculations are done are evenly spaced in logarithmic space in energy, and linearly in redshift. A flat  $\Lambda$  cold dark matter cosmology is assumed in the calculation, with darkenergy density  $\Omega_{\Lambda}=0.73$ , matter density  $\Omega_{M}=0.27$ , and Hubble constant  $H_{0}=70~\mathrm{km~s^{-1}~Mpc^{-1}}$ . The EBL number density  $\eta_{\mathrm{EBL}}$  is scaled with redshift as  $(1+z)^{3-f_{\mathrm{evo}}}$  (Madau & Phinney 1996), and a value of  $f_{\text{evo}} = 1.7$  (evolution factor) is chosen following Abeysekara & Archer (2019), where they find it to be consistent with the Franceschini et al. (2008),

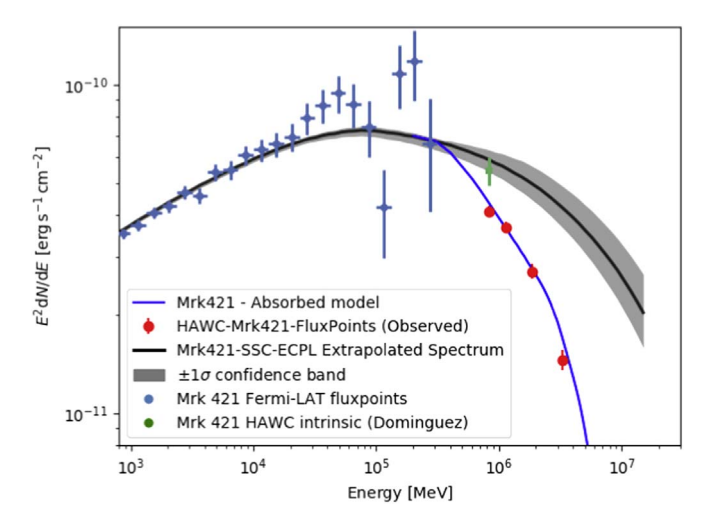


Figure 2. Extrapolated intrinsic emission spectrum for Mrk 421 (black line) along with the  $\pm 1\sigma$  confidence band (statistical uncertainty only). Also shown, are the resulting absorbed spectrum (blue line) according to a random EBL model along with HAWC data, the flux points resulting from the Fermi-LAT analysis (light-blue points), and the de-absorbed HAWC flux point (green) according to the Franceschini et al. (2008) EBL model.

Domínguez et al. (2011), and Gilmore et al. (2012) EBL models. The evolution factor is more relevant when considering sources with multiple redshifts (e.g., Abeysekara & Archer 2019); in this analysis, given that the sources have similar redshifts and there are more important systematics introduced by the intrinsic spectra assumptions, the redshift evolution factor can be considered a subdominant systematic (see Section 4.1). The calculated opacity for each redshift energy is then used to simulate the absorption process by applying the attenuation factor to the assumed intrinsic differential flux in the following way:

$$\frac{dN}{dE_{\text{obs}}} = \frac{dN}{dE_{\text{int}}} \times e^{-\tau(E,z)}.$$
 (3)

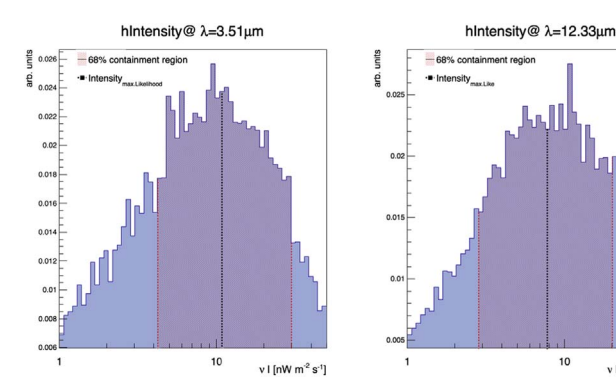
 $\frac{dN}{dE_{\rm obs}} = \frac{dN}{dE_{\rm int}} \times e^{-\tau(E,z)}.$  where  $\frac{dN}{dE_{\rm obs}}$  is the observed differential flux and  $\frac{dN}{dE_{\rm int}}$  assumed intrinsic differential flux.

Figure 2 shows Mrk 421 Fermi-LAT flux points with their corresponding Naima-SSC fit extrapolated into teraelectronvolt energies. An example of the absorbed spectrum according to an EBL model along with HAWC data is also shown.

## 3.3. threeML Framework, Likelihood, and Limit Extraction

The comparison between the expected absorbed model and HAWC data, is performed by adopting a Bayesian approach and using threeML: the Multi-Mission Maximum Likelihood framework, Vianello et al. (2015), Younk et al. (2015). This analysis pipeline is capable of handling data from a wide variety of astrophysical detectors. In this particular study, the HAWC plugin (HAL<sup>35</sup>) is used. The HAL fitting technique is based on a forward-folding method that assumes a spectral model shape for the source. In this case, an SSC source emission model is built using the astromodels package: a useful framework to define models for likelihood or Bayesian analysis of astrophysical data (Vianello et al. 2021). This emission model is customized for each source by plugging in the fit parameters obtained from the Naima fit described in

https://github.com/threeML/hawc\_hal



**Figure 3.** Weighted intensity distributions for  $\lambda = 3.5$  and 12.3  $\mu$ m. The red hatching corresponds to the 68% containment region. The black-dashed line represents the intensity corresponding to the maximum-likelihood model at that particular value of  $\lambda$ .

ν I [nW m<sup>-2</sup> s<sup>-1</sup>]

Section 3.1, to create an intrinsic spectrum that serves as an input for the threeML fitting pipeline. The EBL absorption is applied to the emission model while their spectral parameters are kept fixed. Finally, the forward-folding method, including detector response effects, is performed to fit the absorbed spectrum of the source using a maximum-likelihood technique (Younk et al. 2015) to calculate a likelihood value for the fit  $(\mathcal{L})$ . The process is repeated for each of the 30,000 EBL models generated as explained in Section 3.2. In this way, instead of optimizing the parameters of the source to find the ones that give the maximum likelihood, these are kept fixed, and only the EBL models are evaluated by their ability to reproduce the data. After the test, each EBL model is assigned a likelihood value that quantifies the agreement between that particular emission + absorption model and the actual data. The maximum-likelihood value corresponds to the EBL model whose simulated absorption best reproduces HAWC observations. Starting from a prior flat intensity distribution for each wavelength, resulting from the uniform sampling described in Section 3.2, each model intensity is then assigned a weight as follows:

$$W_i = \frac{\mathcal{L}_i}{\mathcal{L}_{\text{max}}},\tag{4}$$

where  $\mathcal{L}_i$  is the likelihood value corresponding to the *i*th EBL model. The intensities corresponding to the *maximum-like-lihood* model are then assigned a weight of 1 and the rest of the model intensities are weighted by a factor of  $\mathcal{L}_i/\mathcal{L}_{\text{max}}$ , disfavoring EBL shapes that differ from the EBL model that best agrees with the data. This approach is based on the idea of *relative likelihood*, which is an estimate of the probability of a model reproducing data, normalized by the maximum-likelihood value (Kalbfleisch 1985). When combining the results from both sources, each EBL model is weighted by multiplying the individual source weights previously calculated:  $W_{\text{Mrk421}} \times W_{\text{Mrk501}}$ . For each  $\lambda$  value, the maximum-likelihood EBL models from each source are used to calculate an average intensity value for the combined result.

A projection of the EBL intensity probability for each value of  $\lambda$  can be obtained from the histogram of weighted intensities, which represents the posterior distribution of intensities at that  $\lambda$  given the observed data. Figure 3 shows an example of these distributions for two values of  $\lambda$ . The distributions are initially (pre-weighting) flat on average, but

fluctuate in accordance with the random sampling described in Section 3.2. This explains why the intensity corresponding to the maximum-likelihood model (black-dashed line in Figure 3), despite having the greatest weight, does not necessarily correspond with the maximum of the distribution.

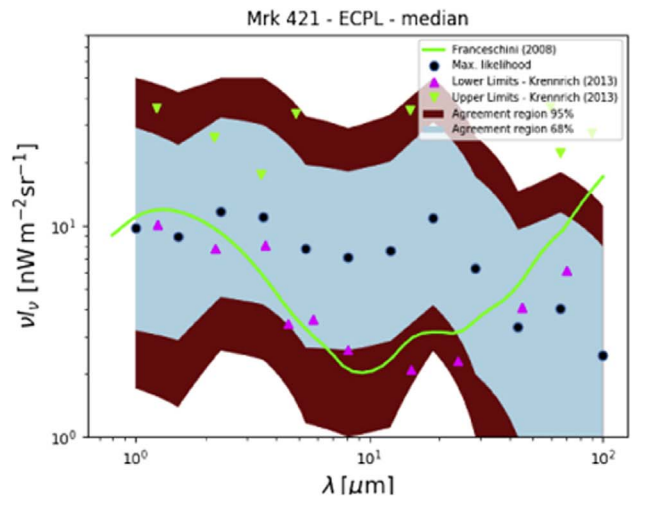
The credible intervals (analogous to confidence intervals in frequentist statistics) are obtained by integrating the 0.68 and 0.95 containment regions from the  $\lambda$  value corresponding to the maximum-likelihood model outward. In this way, the 68% and 95% containment regions are defined around the model that best reproduces the data. For some wavelength values, the corresponding distributions are such that the limits fall outside the considered range of intensity. For these cases, the containment region is reported without a lower/upper boundary. To test the sensitivity of the method to the prior assumptions, the procedure is repeated varying the smoothing condition between consecutive knots and alternatively sampling a flat distribution in the logarithm of the intensities instead of the original linear sampling (see Section 3.2). No significant changes are observed throughout the process with respect to the original prior conditions.

### 4. Results and Discussion

The containment regions are calculated assuming SSC emission models from ECPL-leptonic distributions for both the Mrk 421 and Mrk 501 intrinsic spectral models, as explained in Section 3.1. Figure 4 shows the resulting 68% and 95% containment regions for each of the considered sources as a function of wavelength. The intensities corresponding to the model with the highest likelihood are shown in black circles, along with lower limits from galaxy counts and upper limits from direct measurements shown as upward and downward triangles, respectively.

Figure 5 shows the resulting 68% and 95% containment regions when combining the results from both sources. The combined intensities from each source's highest likelihood model are shown in black circles along with results from other experiments (Abeysekara & Archer 2019; Acciari & Ansoldi 2019; Abdalla et al. 2017). Everything else in the plot is identical to what is shown in Figure 4. From Figure 5 it is clear that for some  $\lambda$  values, namely, 30  $\mu$ m <  $\lambda$  for Mrk 421 and  $\lambda$  < 4  $\mu$ m  $\cup$  10  $\mu$ m <  $\lambda$  for Mrk 501, boundaries cannot be established (see Section 3.3), as limits in these cases are not reported (these are shown as a dash in Table 2).

The containment bands are in good agreement with the region delimited between the lower and upper limits from galaxy counts and direct measurements, respectively. However, for wavelengths lower than  $\lambda = \sim 5 \,\mu\text{m}$ , the containment region is broader than the limits, so the results are nonconstraining in this range. Combined results show a general downward tendency in the EBL measurement for  $\lambda$  values >5  $\mu$ m, following the lower limits from galaxy counts. This downward trend has been observed also by VERITAS (Abeysekara & Archer 2019) and MAGIC (Acciari & Ansoldi 2019). In the case of HAWC, a contributing factor to this trend could be the fact that the highest observed data points (>7 TeV), especially for Mrk 501, seem to show an apparent hardening (see Albert et al. 2022), yielding to lower EBL density values for this wavelength range. However, this hardening comes from flux points that have relatively large statistical errors and could be due to a forward-folding artifact, also seen in other blazar studies (van den Berg et al. 2019).



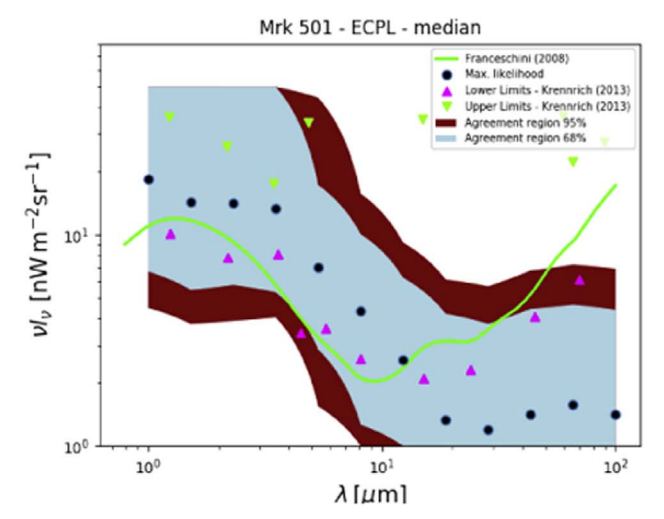


**Figure 4.** 95% and 68% containment bands for the EBL intensity and different  $\lambda$  values. Red circles correspond to the intensities of the model with the highest likelihood value. Also shown, are lower limits from galaxy counts (cyan triangles), upper limits from direct measurements (green triangles), and the Franceschini et al. (2008) EBL model for reference.

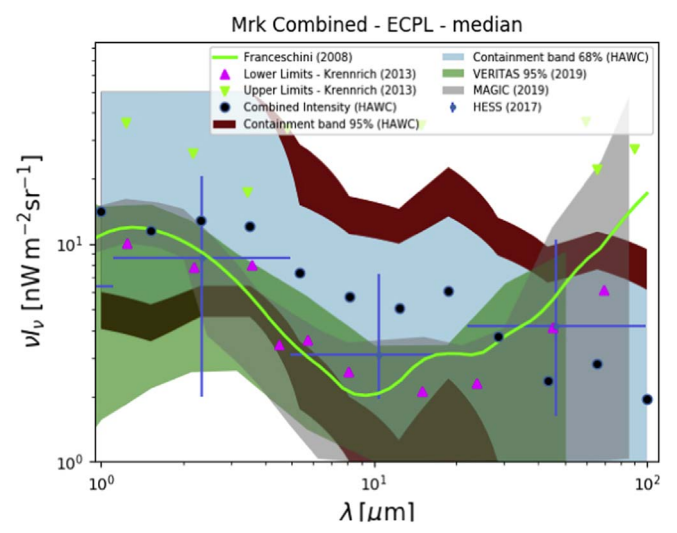


Figure 5. 95% and 68% containment bands for the EBL intensity different  $\lambda$  values for the combined results from Mrk 421 and Mrk 501. Red circles correspond to the combined intensities from each source's highest likelihood models (see Section 3.3). Also shown, are lower limits from galaxy counts (cyan triangles), upper limits from direct measurements (green triangles), and EBL measurements from VERITAS (Abeysekara & Archer 2019), MAGIC (Acciari & Ansoldi 2019), and H.E.S.S. (Abdalla et al. 2017).

HAWC observations of Mrk 421 reported in Albert et al. (2022) point out a power law with an exponential cutoff energy around 5 TeV as the most plausible spectral model for this source. This could, in principle, be related to the bump around 20  $\mu$ m seen in Mrk 421 results (see Figure 4), as in this analysis the EBL shapes are left free, and any decrease in the observed flux will translate into an increase in EBL density for the corresponding wavelength range.

## 4.1. Systematic Uncertainties

There are many sources of systematic uncertainties that affect the flux estimation from HAWC observations, mostly coming from discrepancies between data and simulations, arising from the mis-modeling of the detector. A complete treatment of HAWC possible systematics can be found in Abeysekara et al. (2017) and Abeysekara et al. (2019), in which

	$\nu I_{\min}$ (68%	$\nu I_{\rm max}$ (68%	$\nu I_{\min}(95\%$	$\nu I_{\rm max}$ (95%
$\lambda$	CL)	CL)	CL)	CL)
$\mu\mathrm{m}$	$nW m^{-2} sr^{-1}$	$nW m^{-2} sr^{-1}$	$nW m^{-2} sr^{-1}$	$nW m^{-2} sr^{-1}$
1.0	6.68		4.49	
1.52	5.64	•••	4.01	•••
2.31	6.68	•••	4.76	•••
3.51	6.31	•••	4.49	•••
5.34	3.79	15.48	2.28	•••
8.11	2.28	10.76		15.41
12.33	1.71	9.79	•••	14.02
18.74	2.7	12.74		19.91
28.48		8.36	•••	11.87
43.29		6.2		8.73
65.79		7.24	•••	10.46
100.0		5.59	•••	8.2

Note. An ellipsis indicates that a limit could not be established.

they found that the dominant systematic uncertainties for the spectral flux come from mis-modeling the late light in the air shower and the uncertainty in the modeling of the PMT efficiencies and the charge measured by the PMTs. To estimate the potential effect of these systematics in the overall results, the analysis is repeated simulating extreme detector responses considering these dominant systematics. The results in each case are compared with the nominal results. Figure 6 shows the relative difference for each wavelength between each considered systematic and the nominal results quantified in the following manner:

$$\Delta = \frac{\nu I_{\nu}^{\text{nom}} - \nu I_{\nu}^{\text{sys}}}{\sqrt{\sigma_{\text{nom}}^2 + \sigma_{\text{sys}}^2}},\tag{5}$$

where  $I_{\nu}^{\text{nom}}$  and  $I_{\nu}^{\text{sys}}$  are the EBL density values, at each wavelength, resulting from the nominal model and the considered extreme systematic model, respectively;  $\sigma_{\text{nom}}^2$  and  $\sigma_{\text{sys}}^2$  are the corresponding errors, at each wavelength, for the nominal and systematic results, respectively.

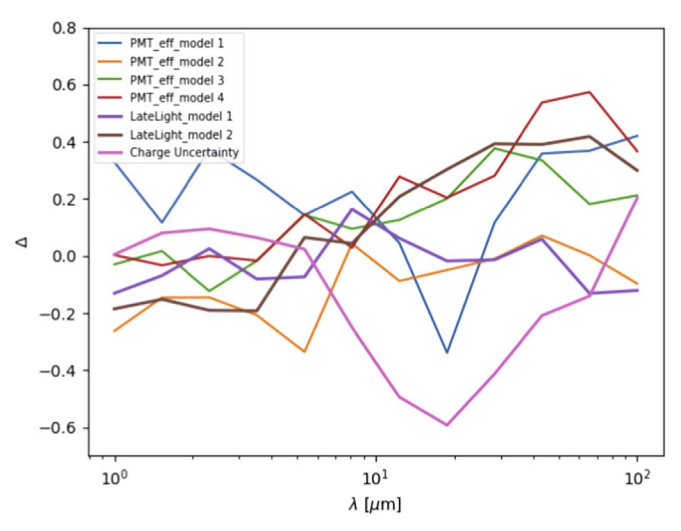


**Figure 6.** Relative difference between the results considering extreme systematics and the nominal results for different values of wavelength  $(\lambda)$ . The meaning of  $\Delta$  is given by Equation (5).

No significant  $(\Delta > 3)$  difference is observed between the results of the nominal model and those when considering extreme systematics. It is important to note that the fact systematics are not significant is, in this case, mostly due to the relatively large errors associated with the method, rather than the instrumental uncertainty being small.

#### 4.2. Intrinsic Model: Potential Bias

The selection of a particular emission model, magnetic field, and emission radius (see Section 3.1) introduces a bias that will eventually impact the calculated EBL limits. As mentioned in Section 3.1, the choice of the parameter values and model is based on previous studies performed on Markarians (Albert et al. 2022; Zhu et al. 2016; Abdo & Ackermann 2011). To estimate the potential bias coming from the selection of the emission model, the analysis was repeated using an electron distribution following a broken power-law (BPL) function instead of the exponentially cutoff power law. In addition, two models following the contours of the  $\pm 1\sigma$  confidence band (see Figure 2) given by the fit described in Section 3.1, are also considered. These latter models are obtained by sampling the fit parameters of the nominal model within their corresponding  $\pm 1\sigma$  errors and retrieving the minimum and maximum flux values for different values of energy. These flux points are then refitted using Naima to get the corresponding parameters of the  $\pm 1\sigma$  models to be used in the analysis in a way analogous to that performed with the nominal model.

The analysis described in Section 3 is repeated for these  $\pm 1\sigma$  models and the corresponding results are used to quantify the overall effect of the intrinsic uncertainties in the final containment bands. Figure 7 shows the relative difference in the derived limits when considering these models with respect to the nominal model and computed as in Section 4.1 by using Equation (5). No significant change is observed between the results of the nominal model and the ones resulting from assuming the  $\pm 1\sigma$  models and assuming the BPL lepton distribution. This suggests that potential biases introduced by the assumptions in the intrinsic emission model do not have a significant impact on the final results within this wavelength range.

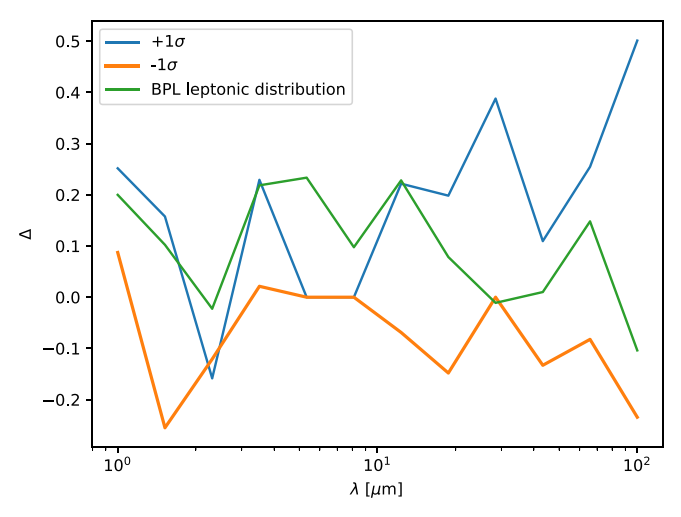


**Figure 7.** Relative difference between  $\pm \sigma$  models, the alternative emission model with a BPL leptonic distribution and the nominal model, for different wavelengths ( $\lambda$ ). The meaning of  $\Delta$  is given by Equation (5).

### 5. Conclusions

After years of operation, the HAWC Observatory is able to significantly detect extragalactic sources, like the Markarians, up to energies of around 10 TeV. This motivates an analysis that could, in principle, probe the mid-IR region of the EBL, a region that is inaccessible to other gamma-ray instruments. In this study, physically motivated emission models and Fermi-LAT data are used to construct an intrinsic spectrum for each of the Markarians, using the Naima python package. A large number of EBL model shapes are randomly generated and used to obtain observed spectra to compare with HAWC data on the Markarians. The comparison is performed using threeML, in a way that each EBL model can be assigned a likelihood value that expresses the agreement between that particular spectral realization and HAWC data. The present method has the advantage of being independent of any particular EBL shape and assuming physically motivated emission models as intrinsic spectra. The EBL intensity measurements and containment bands are calculated from  $1-100 \mu m$ , probing higher wavelength values than previous measurements performed with VERITAS by using a similar method (Abeysekara & Archer 2019). The results for both sources are in agreement with current upper limits from direct IR observations and lower limits from galaxy counts. Limits are, in general, less constraining for wavelengths below  $\lambda = \sim 5 \,\mu \text{m}$  and there is a downward trend when moving to higher  $\lambda$  values, roughly following the lower limits. This trend is more evident in the case of Mrk 501. A bump around 20  $\mu$ m is observed for Mrk 421, possibly due to a cutoff drop present in the source spectrum around  $\sim 5 \, \text{TeV}$  (Albert et al. 2022). The results are also in agreement with other instruments' EBL intensity estimations reported by H.E.S.S. (Abdalla et al. 2017) and MAGIC (Acciari & Ansoldi 2019).

These results would surely improve their constraining power if more adequate sources were included. HAWC continues collecting data from extragalactic sources that could soon be used to derive EBL limits by applying the present method. The radio galaxy M87 was pointed out by Franceschini et al. (2019) as a good candidate to perform EBL-related studies. At the time of writing, this source was detected at too low a significance to be reliable for the analysis; therefore, it is not included. However, M87 data are being accumulated (Albert et al. 2021)

and will soon provide a significant detection that will make the source useful for this type of analysis.

We acknowledge the support from the US National Science Foundation (NSF); the US Department of Energy Office of High-Energy Physics; the Laboratory Directed Research and Development (LDRD) program of Los Alamos National Laboratory; Consejo Nacional de Ciencia y Tecnología (CONACyT), México, grant Nos. 271051, 232656, 260378, 179588, 254964, 258865, 243290, 132197, A1-S-46288, A1-S-22784, cátedras 873, 1563, 341, 323, Red HAWC, México; DGAPA-UNAM grants IG101320, IN111716-3, IN111419, IA102019, IN110621, IN110521; VIEP-BUAP; PIFI 2012, 2013, PROFOCIE 2014, 2015; the University of Wisconsin Alumni Research Foundation; the Institute of Geophysics, Planetary Physics, and Signatures at Los Alamos National Laboratory; Polish Science Centre grant, DEC-2017/27/B/ ST9/02272; Coordinación de la Investigación Científica de la Universidad Michoacana; Royal Society-Newton Advanced Fellowship 180385; Generalitat Valenciana, grant CIDE-GENT/2018/034; Chulalongkorn University's CUAASC grant; Coordinación General Académica e Innovación (CGAI-UdeG), PRODEP-SEP UDG-CA-499; Institute of Cosmic Ray Research (ICRR), University of Tokyo, H.F. acknowledges support by NASA under award No. 80GSFC21M0002. We also acknowledge the significant contributions over many years of Stefan Westerhoff, Gaurang Yodh, and Arnulfo Zepeda Dominguez, all deceased members of the HAWC Collaboration. Thanks go to Scott Delay, Luciano Díaz, and Eduardo Murrieta for technical support.

Software: Naima (Zabalza 2015), 3ML (Vianello et al. 2015), astromodels (Vianello et al. 2021), ebltable (https://github.com/me-manu/ebltable), fermipy v0.17.3 (Wood et al. 2017).

### **ORCID iDs**

```
A. Albert https://orcid.org/0000-0003-0197-5646
H. A. Ayala Solares https://orcid.org/0000-0002-2084-5049
R. Babu https://orcid.org/0000-0003-3207-105X
E. Belmont-Moreno https://orcid.org/0000-0003-3207-105X
K. S. Caballero-Mora https://orcid.org/0000-0002-4042-3855
T. Capistrán https://orcid.org/0000-0003-2158-2292
A. Carramiñana  https://orcid.org/0000-0002-8553-3302
S. Coutiño de León https://orcid.org/0000-0002-7747-754X
E. De la Fuente https://orcid.org/0000-0001-9643-4134
M. A. DuVernois https://orcid.org/0000-0002-2987-9691
M. Durocher https://orcid.org/0000-0003-2169-0306
J. C. Díaz-Vélez https://orcid.org/0000-0002-0087-0693
K. Engel https://orcid.org/0000-0001-5737-1820
C. Espinoza https://orcid.org/0000-0001-7074-1726
K. L. Fan https://orcid.org/0000-0002-8246-4751
M. Fernández Alonso https://orcid.org/0000-0002-6305-3009
N. Fraija https://orcid.org/0000-0002-0173-6453
J. A. García-González https://orcid.org/0000-0002-4188-5584
M. M. González https://orcid.org/0000-0002-5209-5641
J. A. Goodman https://orcid.org/0000-0002-9790-1299
D. Huang https://orcid.org/0000-0002-5447-1786
A. Jardin-Blicq https://orcid.org/0000-0002-6738-9351
V. Joshi https://orcid.org/0000-0003-4467-3621
D. Kieda https://orcid.org/0000-0003-4785-0101
```

J. T. Linnemann https://orcid.org/0000-0003-2696-947X

```
A. L. Longinotti https://orcid.org/0000-0001-8825-3624
G. Luis-Raya https://orcid.org/0000-0003-2810-4867
K. Malone https://orcid.org/0000-0001-8088-400X
O. Martinez https://orcid.org/0000-0001-9052-856X
J. Martínez-Castro https://orcid.org/0000-0002-2824-3544
E. Moreno https://orcid.org/0000-0002-1114-2640
M. Mostafá  https://orcid.org/0000-0002-7675-4656
L. Nellen https://orcid.org/0000-0003-1059-8731
M. U. Nisa https://orcid.org/0000-0002-6859-3944
N. Omodei https://orcid.org/0000-0002-5448-7577
C. D. Rho https://orcid.org/0000-0002-6524-9769
D. Rosa-González https://orcid.org/0000-0003-1327-0838
F. Salesa Greus https://orcid.org/0000-0002-8610-8703
K. Tollefson https://orcid.org/0000-0001-9725-1479
I. Torres https://orcid.org/0000-0002-1689-3945
R. Turner https://orcid.org/0000-0003-1068-6707
F. Ureña-Mena https://orcid.org/0000-0002-2748-2527
E. Willox https://orcid.org/0000-0002-6623-0277
H. Zhou https://orcid.org/0000-0003-0513-3841
```

# References Abdalla, H., Abdalla, H., Abramowski, A., & Aharonian, F. 2017, A&A,

Abdo, A. A., & Ackermann, M. 2011, ApJ, 727, 129

Abdo, A. A., Ackermann, M., Agudo, I., et al. 2010, ApJ, 716, 30

606, A59

```
Abdo, A. A., Ackermann, M., Ajello, M., Baldini, L., & Ballet, J. 2011, ApJ,
Abeysekara, A. U., & Albert, A. 2017, ApJ, 843, 40
Abeysekara, A.U., Albert, A., Alfaro, R., et al. 2019, ApJ, 881, 134
Abeysekara, A. U., Albert, A., & Alfaro, R. 2017, ApJ, 843, 39
Abeysekara, A. U., & Archer, A. 2019, ApJ, 885, 150
Acciari, V. A., & Ansoldi, S. 2019, MNRAS, 486, 4233
Aharonian, F., Akhperjanian, A. G., & de Almeida, U. B. 2007, A&A, 475, L9
Albert, A., Alfaro, R., Alvarez, C., & Camacho, J. R. A. 2022, ApJ, 2, 125
Albert, A., Alvarez, C., Camacho, J. R. A., et al. 2021, ApJ, 907, 67
Biteau, J., & Williams, D. A. 2015, ApJ, 812, 60
Cooray, A. 2016, RSOS, 3, 150555
Domínguez, A., & Primack, J. R. 2011, MNRAS, 410, 2556
Domínguez, A., Primack, J. R., Rosario, D. J., et al. 2011, MNRAS, 410, 2556
Dwek, E., & Krennrich, F. 2013, APh, 43, 112
Elbaz, D., Cesarsky, C. J., Chanial, P., et al. 2002, A&A, 384, 848
Fazio, G. G., Ashby, M. L. N., Barmby, P., et al. 2004, ApJS, 154, 39
Franceschini, A., Foffano, L., Prandini, E., & Tavecchio, F. 2019, A&A,
   629, A2
Franceschini, A., Rodighiero, G., & Vaccari, M. 2008, A&A, 487, 837
Furniss, A., Williams, D. A., Danforth, C., et al. 2013, ApJL, 768, L31
Gardner, J. P., Brown, T. M., & Ferguson, H. C. 2000, ApJL, 542, L79
Gerasimova, N. M., Nikishov, A. I., & Rosenthal, I. L. 1962, JPSJS, 17, 175,
  https://www.osti.gov/biblio/4739582
Gilmore, R. C., Somerville, R. S., Primack, J. R., & Domínguez, A. 2012,
         S, 422, 3189
Gould, R. J., & Schréder, G. P. 1967, PhRv, 155, 1404
Kalbfleisch, J. G. 1985, Probability and Statistical Inference (Springer Texts in
  Statistics), Vol. 2 (Berlin: Springer)
Lagache, G., Puget, J.-L., & Dole, H. 2005, ARA&A, 43, 727
Madau, P., & Phinney, E. S. 1996, ApJ, 456, 124
Madau, P., & Pozzetti, L. 2000, MNRAS, 312, L9
Mazin, D., & Raue, M. 2007, A&A, 471, 439
Orr, M. R., Krennrich, F., & Dwek, E. 2011, ApJ, 733, 77
Papovich, C., Dole, H., & Egami, E. 2004, ApJS, 154, 70
Stecker, F. W., Scully, S. T., & Malkan, M. A. 2016, ApJ, 827, 6
van den Berg, J. P., Böttcher, M., Domínguez, A., & López-Moya, M. 2019,
    nI 874 47
Vianello, G., Burgess, J., Fleischhack, H., Di Lalla, N., & Omodei, N. 2021,
  astromodels, 2.2.2, Zenodo, doi:10.5281/zenodo.5646925
```

Vianello, G., Lauer, R., Younk, P., et al. 2015, ICRC, 34, 1042

Wood, M., Caputo, R., Charles, E., et al. 2017, ICRC, 35, 824

Zhu, Q., Yan, D., Zhang, P., et al. 2016, MNRAS, 463, 4481

Zabalza, V. 2015, ICRC, 34, 922

Younk, P. W., Lauer, R. J., Vianello, G., et al. 2015, ICRC, 34, 948